ARTICLE   OPEN

Check for updates

Heat treatment effects on the corrosion performance of wire arc additively manufactured ER316LSi stainless steel

Corentin Penot [1,2 ✉], Julian Wharton [1], Adrian Addison[3], Yikun Wang[4] and Qing Lu[3]

Corrosion performance of a multi-layered ER316LSi wall deposited using wire and arc additive manufacturing was studied in the as-deposited condition and after stress relief heat treatment at 900 °C, in 3.5 wt% NaCl solution. It was found that the heat treatment is not suitable for WAAM ER316LSi components due to the complete transformation of the delta ferrite into sigma decreasing the corrosion performance. The delta ferrite to sigma transformation during heat treatment was facilitated by the cyclic reheating of the part during deposition. The electrochemical response of as-deposited WAAM differed from a wrought alloy with similar composition and linked to microstructural differences: as-deposited WAAM had a higher pitting potential due to the absence of sulfide inclusions and increased metastable-like activity due to the presence of the secondary delta ferrite causing elemental segregation.

INTRODUCTION

Metallic additive manufacturing (AM) has garnered considerable interest over the past decade due to efforts to enhance manufacture productivity and flexibility, whilst reducing costs. The AM sector utilises a broad variety of processes that build objects from three-dimensional models. Powder-based AM techniques focus on the fabrication of small and complex parts with high precision. However, these powder-based methods are not applicable for larger components due to their slow deposition rates and the need for enclosed working spaces. Direct Energy Deposition processes, such as Wire and Arc Additive Manufacturing (WAAM), are particularly suitable for manufacturing large metallic structures several metres in size[1–5]. WAAM uses an arc welding torch as the deposition head and a welding wire as the feedstock, with a deposition rate between 1 kg h^{-1} and 10 kg h^{-1} depending on the welding torch and the material. Gas Tungsten Arc Welding (GTAW) was initially used to fabricate Ti-6Al-4V components with significant cost reductions[6–10]. GTAW has been utilised for other metals such as Alloy 625 and stainless steels[7,11]. According to Almeida et al.[12], Gas Metal Arc Welding (GMAW) is preferred to GTAW due to its higher deposition rate (i.e. several kg h^{-1} versus 1 kg h^{-1}, respectively). However, arc wandering led to sputtering issues limiting the use of conventional GMAW to deposit Ti-6Al-4V and aluminium alloys. Alternatively, austenitic stainless steels (ASSs) have excellent weldability and are suitable candidates for GMAW WAAM. Among ASSs, stainless steel 316L (UNS S31603) is intensively used in various industry sectors such as maritime, oil and gas, nuclear or chemical processing as machinery parts or structural components for its good mechanical and corrosion performance. Significant gains are expected by employing WAAM with stainless steel 316L, for instance in the marine industry as a highly flexible manufacturing process (i.e. off-the-shelf equipment and portable) capable of rapidly producing and/or repairing large-scale 316L components off-shore. Indeed, stainless steel 316L has been used to produce fully dense and mechanically operational parts using GMAW WAAM[13–23]. The

WAAM microstructures were heavily affected by the deposition process and were highly complex, with anisotropic texturing and an austenite (γ) matrix with a secondary delta ferrite (δ) phase. The microstructural complexity requires a more comprehensive understanding of the material properties before deployment, particularly in corrosive environment such data are limited.

Overall, the AM 316L corrosion performance is linked to the deposition process (i.e. thermal cycling and high cooling rates). For instance, AM via selective laser melting is considered to enhance corrosion performance compared to conventional wrought 316L[24–27], associated with the high cooling rate involved during solidification and the resulting fine cellular structure. However, the corrosion performance of WAAM deposited 316L remains to be fully qualified. Quegueineur et al.[28] reported satisfactory corrosion response for Cold Metal Transfer (CMT, i.e. GMAW variant) deposited 316L (EN X2CrNiMo19-12) compared with a laminated 316L (EN X2CrNiMo17-12-2). Whereas, Wen et al.[29] remarked that elemental segregation of chromium associated with delta ferrite led to an inferior corrosion resistance for CMT deposited 316LN multilayer thin walls. Chen et al[30] produced a 316L plate with GMAW WAAM and reported the presence of sigma phase (σ) at the γ/δ interface, potentially affecting the corrosion resistance[31–34], thus emphasising the critical need to better understand the relationship between the WAAM microstructure and the corrosion performance. Furthermore, AM builds suffer from residual stress that can be harmful to the service properties[35–37]. This is often alleviated by a post-deposition stress relief heat treatment (HT) which is a common practice for ASS parts. HT at 900 °C for 2 h is usually performed to relieve the stress accumulated during the manufacturing process[38]. However, there are few studies on HT effects on the microstructure and corrosion resistance of WAAM 316L deposits. In addition, data for high-temperature post weld heat treatment (PWHT) on 316L is also scarce since its low carbon content generally limits the need for PWHT to avoid sensitisation[39], i.e. sensitisation being the main detrimental phenomenon for

---

[1]National Centre for Advanced Tribology at Southampton (nCATS), Faculty of Engineering and Physical Sciences, University of Southampton, Southampton, UK. [2]The National Structural Integrity Research Centre (NSIRC), Granta Park, Cambridge, UK. [3]TWI Ltd, Granta Park, Cambridge, UK. [4]Lloyd's Register EMEA, Global Technology Centre, Hampshire House, Hampshire Corporate Park, Eastleigh, UK. ✉email: c.penot@soton.ac.uk

mechanical properties and corrosion resistance of weldments. Nevertheless, it is well-known that intermetallic sigma phase can precipitate from delta ferrite within 316L welds between 600 °C and 900 °C; however, the precipitation rate decreases after 800 °C[40,41]. Raghunathan et al.[42] showed that HT of type 316 stainless steel welds at 900 °C for less than 2 h only resulted in a slight decrease in the delta ferrite content without the precipitation of intermetallic phase, thus suggesting HT could be performed on WAAM ER316LSi deposits without precipitating intermetallic phases. Despite similarities, WAAM ER316LSi is microstructurally dissimilar to conventional 316L welds and the suitability of stress relief HT of WAAM ER316LSi remains to be fully established. As such, this work aims to provide insights into WAAM corrosion mechanisms, for as-deposited, and after a stress HT. The study fabricated a multi-layered GMAW WAAM ER316LSi wall. The effects of a post-fabrication stress relief HT (2 h dwell at 900 °C) on the microstructure and corrosion performance were assessed and compared to as-deposited (AD) specimens, as well as conventional wrought 316L specimens.

RESULTS

Material characterisation

The WAAM ER316LSi as-deposited (AD WAAM) dendritic micro-structure is shown in Fig. 1a, b, with the dendrites oriented in the y-direction (build direction). Two phases are visible, the light grey phase is identified as austenite (matrix) and the dark grey phase as delta ferrite (secondary phase). The individual AM deposition layers are clearly visible, with the dendrite size varied gradually within the layers, resulting from the multiple thermal cycles that lead to complex cooling rates and re-heating during the WAAM wall fabrication. The re-heating of the exposed top region by the subsequent layer deposition coarsens the dendrites below the layer transition (heat affected zone—HAZ), whereas the fine dendrites are formed within the new layer, indicating a higher cooling rate, as the material re-melted and re-solidified instantly as suggested by the ripples still visible at this location (remelting zone). Dendrites solidify by epitaxial growth from existing layer occasionally growing across multiple layers (trans-layer dendrite). The delta ferrite was predomi-nantly reticular with occasional lathy clusters. AD WAAM mid-layer EBSD mapping confirmed the presence of an austenite matrix with delta ferrite as the secondary phase, as seen in Fig. 1c. Furthermore, minor amounts of sigma phase (<1%) were detected at the interface between the austenite and ferrite phase. The crystallographic orientation map provided in Fig. 1d revealed long columnar grains oriented towards the y-direction and the dendrite growth direction. The crystal lattice is preferentially 001 oriented with respect to the build direction. As anticipated, the deposited 316LSi microstructure is strongly anisotropic. Figure 2 shows the heat-treated WAAM ER316LSi (HT WAAM) microstructure. Overall, there are similarities
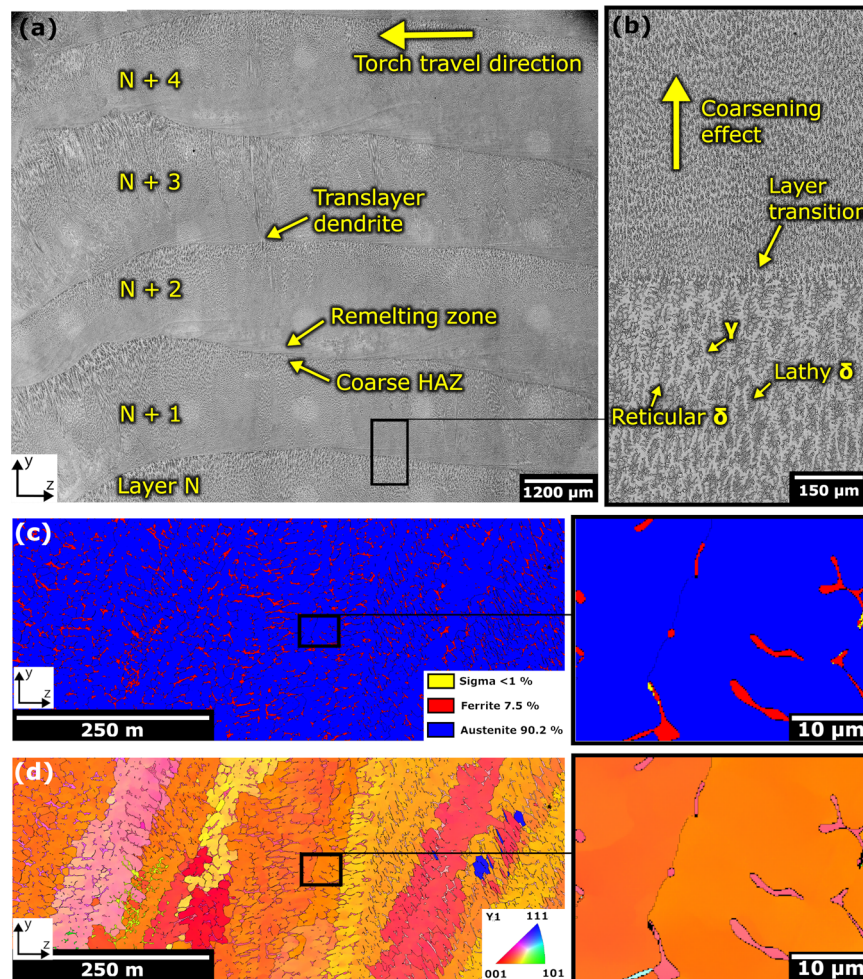

Fig. 1 Microstructure of the as-deposited WAAM 316LSi. a Optical microscopy of the etched as-deposited WAAM 316LSi cross section (vertical orientation). Five layers are visible and are labelled N to N+4; **b** higher magnification of the layer transition between N and N+1, dendrites transition from coarse at top N to fine at bottom N+1 layer. Mid-layer EBSD of the as-deposited WAAM 316LSi; **c** phase maps and **d** crystallographic orientation with respect to build direction (y).
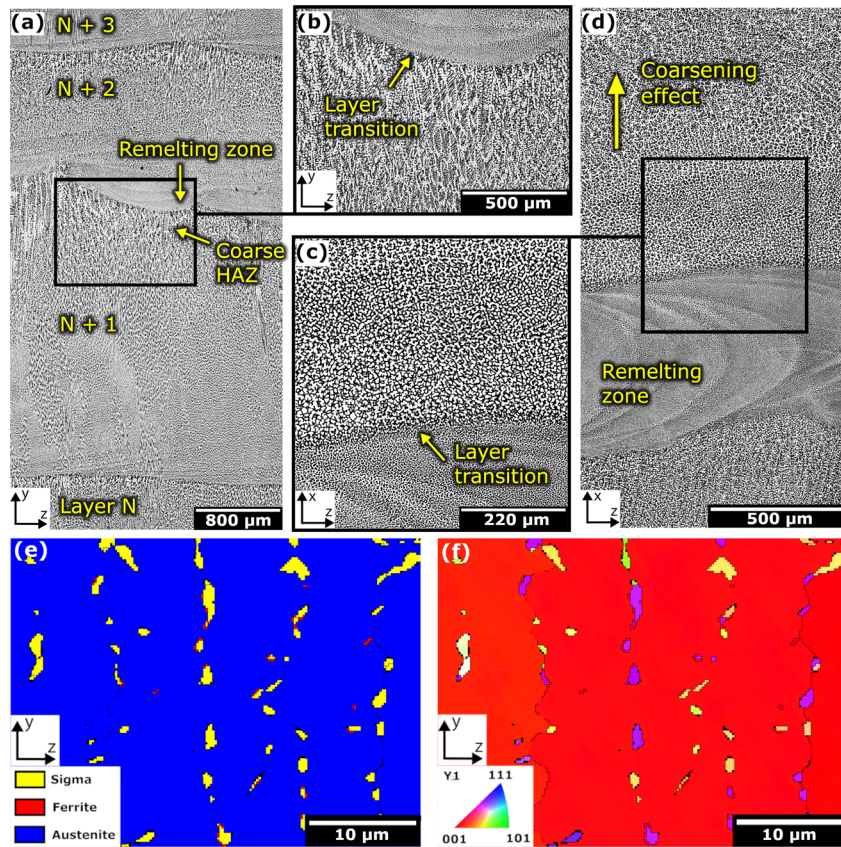
Fig. 2 Microstructure of the heat-treated WAAM 316LSi. Optical microscopy of the etched heat-treated WAAM 316LSi; **a** cross section - (y, z) plane; **b** interlayer zone. **d** Horizontal - (z,x) plane **c** interlayer zone from **d**. mid-layer EBSD of the heat-treated WAAM 316LSi; **e** phase maps and **f** crystallographic orientation with respect to build direction (y).

with the dendritic microstructure observed in the AD WAAM. The WAAM deposition features are still visible and the same coarsening effect is clearly evident within the deposited layers. The EBSD map of the heat-treated identifies the secondary phase as sigma phase in Fig. 2e. Feritscope measurements confirmed the ferrite contents as 10 ± 1.0% and 1.5 ± 0.9%, for the AD and HT WAAM, respectively. The sigma content after HT was evaluated via a comparative analysis of the secondary phase content obtained from SEM and Feritscope measurements. The resulting estimate of the sigma content was determined to be 8.9 ± 1.3%. This implies that a vast majority of the delta ferrite, ~85%, underwent an exclusive transformation into sigma during the specified heat treatment. Furthermore, the secondary phase observed in Fig. 2 (appearing as dark grey) is primarily comprised of sigma. The grain crystal lattice visible in the crystallographic orientation map Fig. 2f is still 001 oriented with respect to the build direction.

Semi-quantitative EDX line scans were performed to assess the distribution of relevant elements such as Cr, Mo, and Ni across the three microstructural interfaces found in AD and HT WAAM 316LSi: ferrite/austenite (Fig. 3a), ferrite/austenite/sigma (Fig. 3b), and sigma/austenite (Fig. 3c).

As an austenite stabiliser the Ni content was higher in the matrix at around 12.7 wt% and decreased below 7 wt% in the delta ferrite and sigma phase. The Cr content was higher in the ferrite and in the sigma phase than in the austenite matrix. This was expected since Cr is known as a ferrite stabiliser and sigma is a Cr-Mo-rich intermetallic phase. In all three cases, the Cr content was above 23 wt% in the sigma and ferrite phases, and it was approximately 17.8 wt% in the austenite phase. Similarly, the Mo content was higher in the ferrite and sigma phases compared to the austenite matrix since Mo is also a known ferrite stabiliser.

The Mo content in the ferrite phase was between 3.6 wt% and 4.2 wt%, whereas it was higher in the sigma phase ranging between 5.3 wt% and 5.8 wt%. Note that the electron beam spot size limits the measurement of the ferrite or sigma phase. There will be contributions from adjacent phases especially near boundaries. Likewise, another variability is the depth of the analysed region. The local phase needs to be deeper than the beam penetration distance. This is not an issue with the austenite matrix where there is sufficient confidence that the beam only analyses the austenite. Therefore, the Cr content in the austenite phase is relatively consistent at 17.8 wt%. However, the austenite Mo content varies from 2.4 wt% in the absence of sigma, to 2.2 wt% with a low sigma content (AD WAAM), and 1.8 wt% with a high sigma content (HT WAAM). It is interesting to note that the UNS S31600/S31603 standard specifies a minimum of 2.0 wt% Mo. The analysis resolution in this instance was not able to detect Cr- and Mo-depletion zones within the austenite phase immediately adjacent to either ferrite or sigma phases. Further studies are needed to establish the extent of any depletion zones.

Numerous inclusions are present as black spherical features in Fig. 3. The spherical shape suggests a rapid precipitation and the inclusion diameter distribution is shown in Supplementary Fig. 1. Most inclusions were sub-micron (typically 0.25 μm in diameter) confirming a rapid precipitation during the solidification stage that prevented further growth. EDX analysis indicates aluminium- and manganese-rich silicates, with traces of sulfur (S), titanium and magnesium. Identical inclusion compositions and size were evident for both AD and HT WAAM 316LSi specimens, as shown in Supplementary Fig. 1. Interestingly, no manganese sulfide (MnS) inclusions were found in either of the WAAM specimens. The current status of WAAM relies on commercially available welding
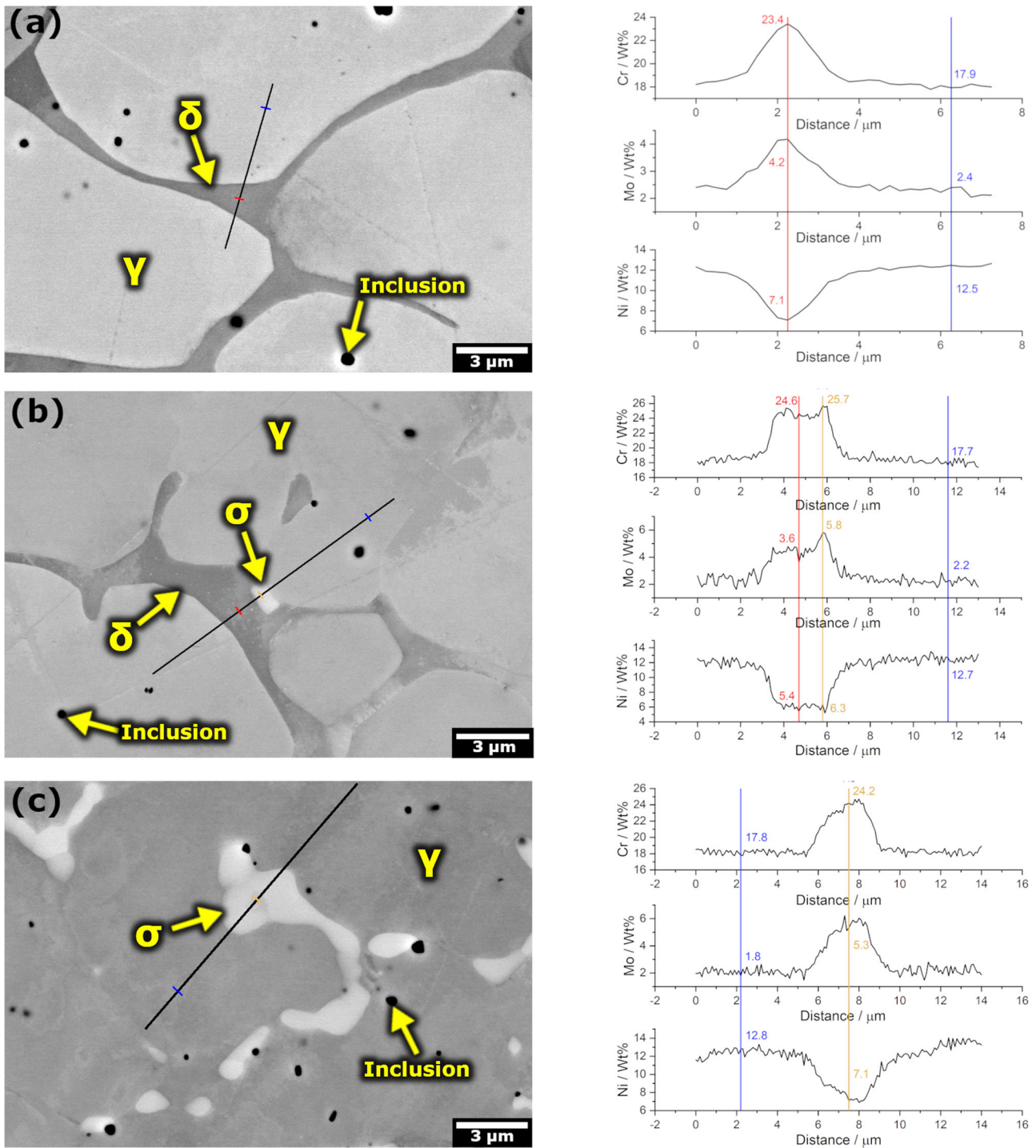
Fig. 3 **EDX line analysis across phase interfaces.** EDX line analysis for: **a** ferrite/austenite interface in the as-deposited WAAM 316LSi; **b** ferrite/austenite/sigma interfaces in the as-deposited WAAM 316LSi; **c** austenite/sigma interface in the heat-treated WAAM 316LSi.

wires enriched in Si and Mn, similar to the one used in this study. These elements act as deoxidisers and capture impurities such as sulphur, phosphorus, and oxygen present in the melt, forming manganese silicate inclusions and compounds composed of MnO $-SiO_2(-Al_2O_3-TiO_3-CaO-MnS)$[43,44] at high temperatures exceeding the solidus temperature. The primary inclusion thus formed serves as the precursor for MnS precipitation during cooling. Si increases the solubility of S in the primary oxides, impeding MnS precipitation[43]. Prior studies have reported the presence of nano-sized MnS within primary manganese silicate

inclusions in WAAM-deposited 316L SS, which corresponds to the initial stage of MnS precipitation as previously described[23,45]. A single inclusion of this type was found in the HT specimen, and its image is presented in Supplementary Fig. 2. A higher concentration of S was detected in small sub-inclusions at the edge of the primary manganese silicate inclusion, indicating the possibility of MnS precipitation. However, the small size (<0.18 μm) of these sub-inclusions, as well as their embedded position within the primary manganese silicate, suggest incomplete precipitation and confirm that the cooling rates prevent MnS formation due to
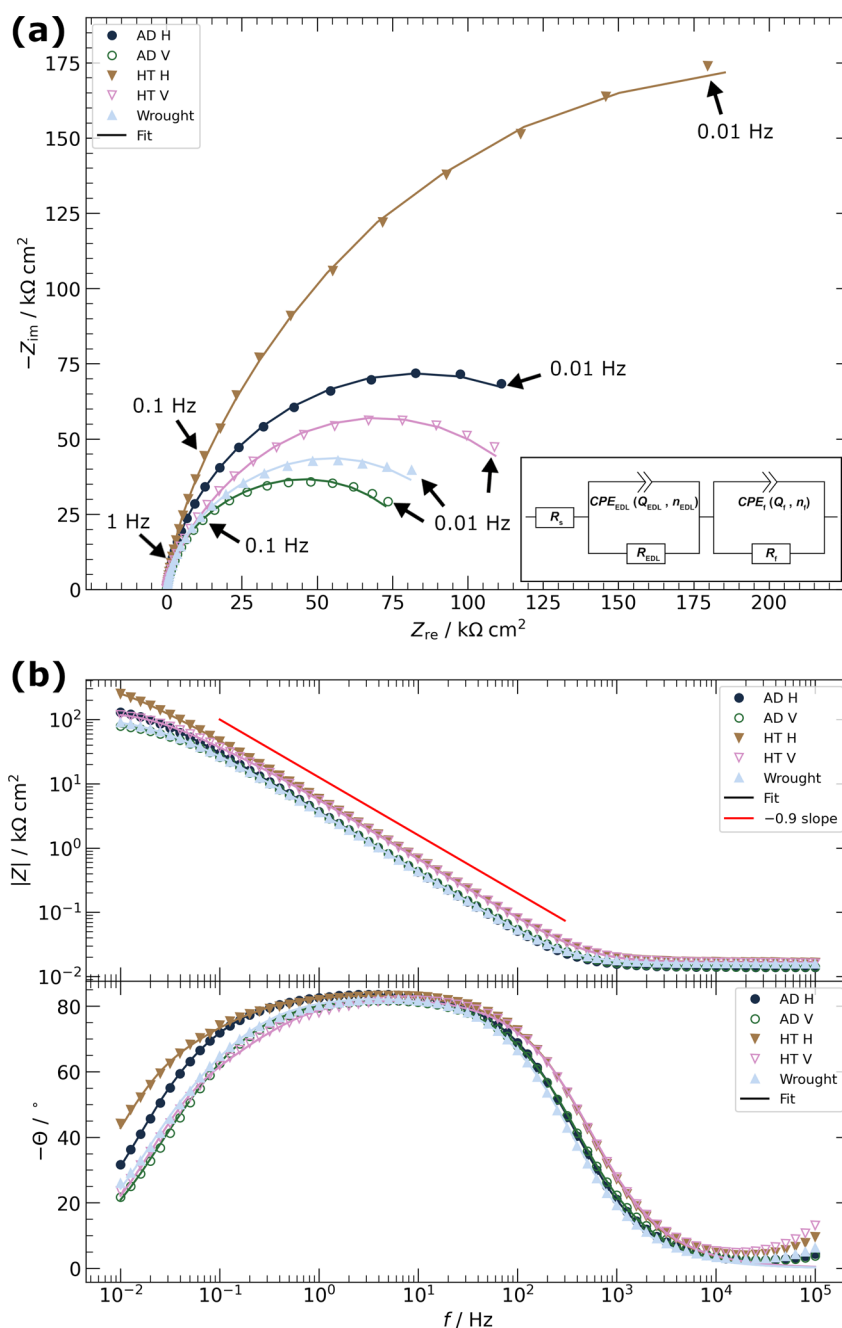
Fig. 4 EIS data plots. EIS data for as-deposited WAAM 316LSi, heat-treated WAAM 316LSI and wrought 316L stainless steel in a 3.5 wt% NaCl test solution (after 1 h immersion, at OCP −0.159, −0.163, −0.155, −0.166 and −0.173 V vs. Ag/AgCl, for AD H, AD V, HT H, HT V and wrought, respectively): **a** Nyquist plots and the inset shows the equivalent circuit used to model the data, **b** Bode impedance modulus ($|Z|$ *vs.f*), and Bode phase angle (θ vs. *f*) at OCP.

insufficient diffusion time[46,47]. No pores were found in the deposited wall. The compacity of WAAM fabricated ASS is high and porosity or lack-of-fusion are rarely reported with appropriate deposition parameters[21,48,49].

Electrochemical performance

Electrochemical tests were conducted on the wrought 316L, horizontal (z, x) AD WAAM (AD H), vertical (y, z) AD WAAM (AD V), horizontal (z, x) HT WAAM (HT H), and vertical (y, z) HT WAAM (HT V) 316LSi stainless steel specimens to determine the corrosion performance. Inevitably there will be an inherent stochastic character of the WAAM surfaces governed by the exposed

microstructure and its electrochemical response. The EIS Nyquist and Bode plots are shown in Fig. 4 (plus the fitted model data— solid lines). The EIS data all have a similar form indicating a consistent metal/solution response. The Nyquist plots (Fig. 4a) have different arc diameters which are often associated with a capacitive behaviour of the electrical double layer (EDL) and passive film[50,51]. The capacitive arcs are distorted semi-circles, suggesting the overlapping of two capacitive systems (or time constants). The Bode plots (Fig. 4b) show three distinct regions at high, intermediate and low frequency. The low-frequency region (between 0.01 Hz and 0.1 Hz) is associated with slow processes, for instance charge transfer across the metal/solution interface and is often representative of the polarisation resistance (R_p). The

Table 1. EIS fitting parameters (percentage error are indicated within brackets), LPR and PDP values.

Specimen	EIS fitting parameters										LPR	PDP		
	R_s / Ω cm²	R_{EDL} / kΩ cm²	Q_{EDL} / MΩ⁻¹ cm⁻² sⁿ	n_{EDL}	$C_{eff,\,EDL}$ / μF cm⁻²	R_f / kΩ cm²	Q_f / MΩ⁻¹ cm⁻² sⁿ	n_f	$C_{eff,\,f}$ / μF cm⁻²	χ^2 (10⁻⁴)	R_p / kΩ cm²	E_{corr} / V	j_{pass} / μA cm⁻²	E_{trans} / V
Wrought	16.5 (0.9)	65 (2.4)	47 (0.8)	0.92 (0.2)	25 (5.0)	165 (7.6)	132 (2.0)	0.96 (0.5)	150 (1.6)	2.1	198	−0.212 ± 0.059	0.44 ± 0.14	0.372 ± 0.007
AD H	16.9 (0.8)	56 (2.8)	62 (0.8)	0.91 (0.2)	32 (4.8)	96 (3.6)	117 (1.5)	1.00 (0.5)	117 (0.6)	1.7	125	−0.241 ± 0.022	0.64 ± 0.24	0.545 ± 0.014
AD V	16.8 (0.8)	39 (2.4)	68 (0.8)	0.9 (0.2)	32 (5.0)	64 (2.9)	117 (1.4)	0.97 (0.4)	124 (1.4)	1.4	92	−0.255 ± 0.006	0.63 ± 0.12	0.524 ± 0.017
HT H	19.8 (1.0)	434 (3.5)	36 (0.8)	0.94 (0.2)	22 (5.1)	21 (10)	103 (2.5)	0.91 (0.5)	112 (6.6)	2.2	446	−0.246 ± 0.039	0.39 ± 0.18	0.486 ± 0.033
HT V	19.4 (1.0)	146 (2.2)	41 (0.9)	0.93 (0.2)	24 (5.1)	12 (6.9)	83 (2.1)	0.93 (0.4)	82 (5.6)	2.2	142	−0.191 ± 0.047	0.43 ± 0.13	0.326 ± 0.022

E_{pit} is averaged from triplicate tests available in Supplementary Fig. 4.

intermediate frequency region (between 0.1 Hz and 1000 Hz) confirmed the capacitive behaviour since the Z to frequency slope was close to −1 (around −0.9 for all specimens—see red line in Fig. 4b) and phase angles of −80°[50]. Additionally, the phase angle plateau between 0.1 Hz and 100 Hz is also indicative of two distinct capacitive systems[51]. At high frequencies (≥1000 Hz), charge transfer processes across the metal/solution interface are too slow to occur and the capacitive behaviour of the interface predominates. Thus, the impedance is governed by internal resistances, in this instance the solution resistance (R_s). EIS data were modelled using an equivalent circuit of the surface phenomena occurring at the interface to obtain further insights regarding the physical structure of the metal/solution interface.

A rationale for the equivalent circuit model selection can be found in Supplementary Note 1. The selected model divides the passive film into two contributions: an outer hydroxide layer combined with the EDL (i.e. CPE_{EDL}, R_{EDL}), and an inner oxide layer (i.e. CPE_f, R_f). The two-time constants in the equivalent circuit (i.e. oxide and hydroxide/EDL interfaces) are in series and are thus interchangeable. Boissy et al.[52] remarked the smaller capacitance can be associated with the hydroxide and EDL interface (i.e. CPE_{EDL}, R_{EDL}), since the potential difference is greater between the hydroxide and electrolyte than between the oxide and hydroxide. Overall, the two CPEs have behaviours close to an ideal capacitor, thus Q_{EDL} and Q_f can be related to the effective capacitance of their respective system (i.e. hydroxide/EDL and oxide film). The effective capacitance of CPE_{EDL} was assessed using the following formula[53]:

$$C_{eff,EDL} = Q_{EDL}^{1/n_{EDL}} \left(R_s^{-1} + R_{EDL}^{-1} \right)^{(n_{EDL}-1)/n_{EDL}} \tag{1}$$

Whereas, the effective capacitance of CPE_f was determined using an expression used by Hsu and Mansfeld[54] and Hirschorn et al.[55]:

$$C_{eff,f} = Q_f^{1/n_f} R_f^{(1-n_f)/n_f} \tag{2}$$

Qualitatively, the capacitance is inversely proportional to the film thickness considering equivalent dielectric permittivity between specimens[55]. The various fitting parameters and effective capacitances are summarised in Table 1. It is evident the hydroxide/EDL resistance (R_{EDL}) is lower for AD than HT, plus the effective capacitance of the hydroxide/EDL ($C_{eff,EDL}$) was higher for AD than HT, suggesting a thicker hydroxide layer for the latter[55]. The wrought 316L gave a comparable performance to AD for both R_{EDL} and $C_{eff,EDL}$. The inner oxide film resistance (R_f) ranked from lowest to highest was HT, followed by AD and then wrought 316L. The $C_{eff,f}$ indicates that the oxide film is the most compact for wrought 316L, since R_f was higher despite a greater capacitance (i.e. thinner film thickness). WAAM AD and HT had comparable $C_{eff,f}$ suggesting similar film thicknesses; however, the HT specimens had lower R_f indicating a higher defect density. Additionally, n_f values were higher (>0.96) for both wrought and AD than for HT (<0.93), which again suggests that the HT oxide films have a marginally higher defect density. Overall, at OCP, wrought 316L has the most compact and thus protective inner oxide film. The AD WAAM has a less compact oxide film, although when compared with HT WAAM it has a lower defect density and a more protective oxide film. The HT WAAM has the least protective inner oxide film but a higher resistive outer hydroxide layer.

Representative potentiodynamic polarisation curves are shown in Fig. 5, revealing behaviours consistent with a 316 ASS in a NaCl test medium, i.e. a passive region where the current density is low and a passive-active transition at the pitting potential (E_{pit}), followed by an increase in the current density[56]. One notable contrast between wrought and WAAM is the gradual and fluctuating increase in current density after the passive-active transition for the latter. These transients originate from numerous
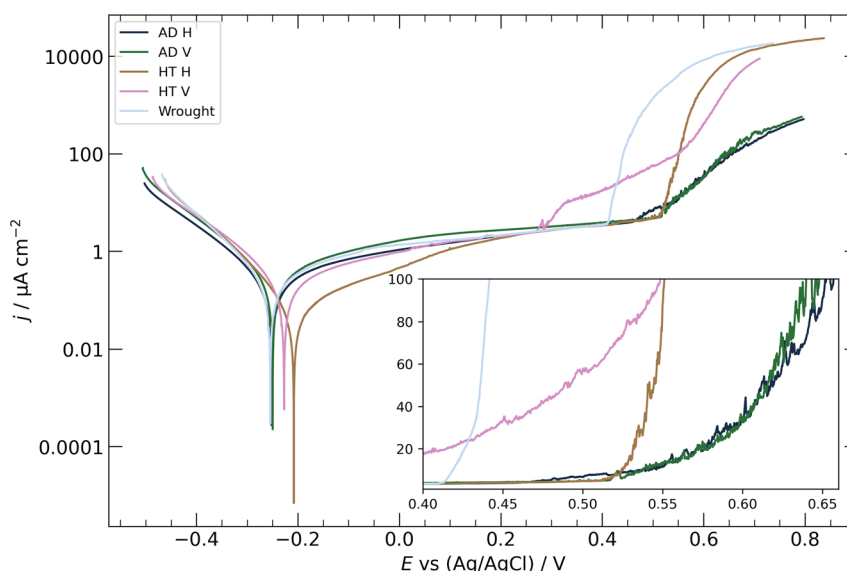
Fig. 5 Potentiodynamic polarisations. Potentiodynamic polarisations of as-deposited WAAM 316LSi, heat-treated WAAM 316LSi and wrought 316L stainless steel in a 3.5 wt% NaCl test solution (scan rate = 0.5 mV s^{-1}). Inset shows the anodic transients for WAAM specimens.

depassivation-repassivation events similar to metastable pit activities. Therefore, the potential of the passive-active transition, E_{trans}, was discussed instead of E_{pit}. E_{trans} is defined as the potential at which the passive film either durably breaks due to stable pitting (characterised by a steep increase in current density) or repeatedly breaks due to frequent metastable-like pit events (slower and fluctuating increase in current density). Metastable pit events typically generate current transients between 4 and 20 μA[57]. Hence, E_{trans} is considered to be reached when the current density transients permanently exceed 10 μA cm^{-2} (13.3 μA, assuming it is caused by a single metastable pit), at which point it is reasonable to assume that complete passivity of the surface has been lost. For polarisation curves where the occurrence of a stable pit is evident, the potential at 10 μA cm^{-2} matches well with the current density increase due to pitting and is therefore also taken as E_{trans}. The corrosion potential (E_{corr}), passive current density (j_{pass}), E_{trans} assessed from PDP, plus the R_p values determined via LPR, are summarised in Table 1 (where j_{pass} corresponds to the current density at E_{corr} +0.100 V). LPR plots are shown in Supplementary Fig. 3. Overall, the LPR-derived R_p values were consistent with the EIS data ($R_{EDL} + R_f$). The HT specimen had the highest R_p and the lowest j_{pass} which is attributed to a more resistive hydroxide layer (as seen from the EIS). However, the gradual passive current increase with increasing potential was more significant for HT H suggesting that the hydroxide layer resistivity decreases at a faster rate than that of the inner oxide film. AD specimens had higher E_{trans} than wrought 316L and E_{trans} for HT H was close to those of AD whereas HT V had the lowest E_{trans}. Furthermore, the current density rise after pitting was less abrupt for AD H, AD V and HT V than for HT H and wrought 316L, suggesting a higher dissolution rate for the latter.

Post-PDP microscopic examinations of both AD V and HT V WAAM samples, as well as wrought 316L, confirmed that WAAM 316LSi had greater metastable-like activity, as depicted in Fig. 6. The surfaces of both AD V (Fig. 6a) and HT V (Fig. 6c) exhibited more evident corrosion features when directly compared with wrought 316L (Fig. 6e). The feature density exceeded 10 mm^{-2} for both AD V and HT V, but was less than 1 mm^{-2} for wrought 316L. The average area of the surface feature was typically 50 μm^2 for AD V and HT V WAAM 316LSi, whereas it was ~360 μm^2 for wrought 316L, indicating a higher proportion of stable pits for the latter while small repassivated metastable-like pits with decreased average size dominated in the former two. These observations

confirm that the PDP fluctuations at high anodic overpotentials for WAAM 316LSi were caused by extensive metastable-like activity, as depicted in the inset of Fig. 5. The dark field reveals the selective dissolution of the austenite phase during pitting of the WAAM specimens, as seen in Fig. 6a, b. The corrosion features developed at the boundary between the secondary phase (dark grey) and the austenite (light grey) suggesting that the metastable-like activity is related to the secondary ferrite microstructure network (evident in the dark-field view). More detailed evidence of the WAAM 316LSI microstructural selective dissolution is presented in Fig. 6g–j where pits initiate and grow within the austenite surrounding the secondary ferrite for AD WAAM (Fig. 6a, b) and around the sigma for HT WAAM (Fig. 6c, d).

DISCUSSION
The complete transformation of delta ferrite to sigma phase during the conventional stress relief heat treatment is unexpected when considering the sigma Time-Temperature Transformation (TTT) diagram in a 316L weldment, see Fig. 7[40]. A 2 h dwell at 900 °C is generally considered to be outside the delta ferrite sigma forming domain and thus should not precipitate sigma. Sigma precipitation during the heat treatment is a likely consequence of the thermal cycles due to the new layer additions during the WAAM 316LSi wall build, which initiate the ferrite transformation in the course of the deposition. The presence of sigma in the AD specimen suggests that it was maintained for a sufficient time within the 600 °C to 900 °C range to initiate the ferrite to sigma transformation[41]. The heat treatment continues the transformation mechanism resulting in the complete transformation of the delta ferrite into sigma (case 3 in Fig. 7). Interestingly, Guilherme et al.[34] reported reheating of previously deposited layers in multi-pass welding can cause sigma formation in Mo containing stainless steels. Chen et al.[13] have also found sigma phase and justified by the reheating of the material by deposition of subsequent layers. The presence of sigma in stainless steel weldments is known to be detrimental to corrosion performance[31–34].

In this study, higher sigma contents within the HT WAAM may have led to the electronegative shift in the E_{trans} seen for HT V or alternatively to an abrupt current density increase at E_{trans} as for the HT H, when compared directly to the AD WAAM. This is linked to the lower Mo content within the austenite matrix (seen by the EDX analysis). The ferrite transformation into the Mo-rich sigma
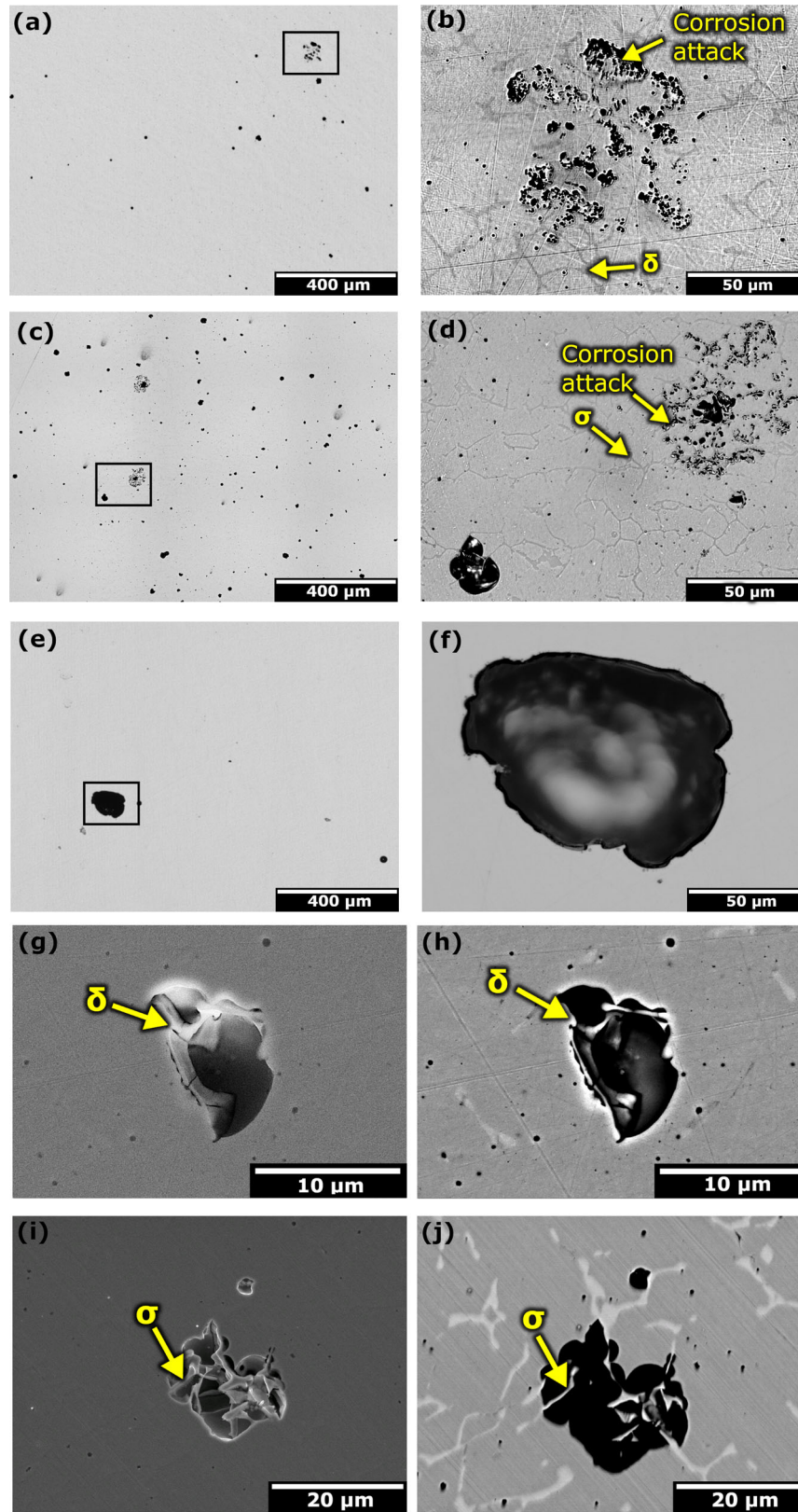
Fig. 6   Post-potentiodynamic polarisation corrosion feature optical microscopy and SEM. Optical microscopy of the AD and HT WAAM 316LSi, and wrought 316L stainless steel post potentiodynamic polarisation: **a** AD V specimen and **b** higher magnification dark field mode; **c** HT V specimen and **d** higher magnification dark field mode; **e** wrought specimen and **f** higher magnification normal mode. SEM of WAAM 316LSi metastable-like pit features post potentiodynamic polarisation: **g** SE and **h** BSE of the AD H specimen; **i** SE and **j** BSE of the HT H specimens.
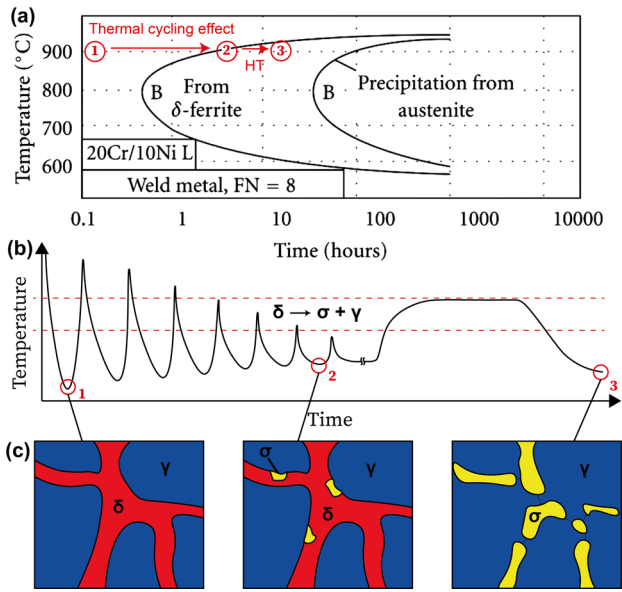
Fig. 7 Schematic of the thermal profile during the WAAM deposition. a TTT diagram for sigma phase in a stainless steel weld (B: initial precipitation)[40], **b** schematic of the thermal profile for a fixed-point during deposition and HT, **c** corresponding microstructure. Highlighted points: (1) after a single pass, (2) after multiple passes and (3) after stress relief HT.

Fig. 8 Illustrations of the underlying corrosion mechanisms during potentiodynamic polarisation. Illustrations of the underlying corrosion mechanisms for wrought 316L and WAAM 316LSi stainless steel during PDP testing.

phase must mean Mo diffuses from the austenite matrix (dealloying). Molybdenum additions to stainless steels are generally considered to affect the anodic pit kinetics, shifting the pitting potential towards more noble potentials (about 70–100 mV)[58]; hence creates a local micro-galvanic cell between the Mo-enriched sigma as the cathode and the depleted austenite matrix as the anode which dissolves preferentially at the vicinity of sigma (see Fig. 6). Insights from the EIS for HT (i.e. low R_f) and the lower E_{trans} from specimen HT V suggest the presence of sigma causes passive film instability at higher potentials. Differences between the nature of the austenite and sigma passive films may lead to surface discontinuities, such as either a defect-rich passive film at the austenite/sigma interface or a chromium depletion zone at these interfaces considering sigma is also Cr-rich.

According to the EIS data, wrought 316L has a more protective passive film than AD WAAM 316LSi; however, local depassivation (i.e. pit initiation and propagation) occurred at lower anodic overpotentials. Additionally, the current density increase after pitting was more abrupt and generated by only a few propagating pits (as corroborated via post-test microscopy). Conversely, for AD WAAM, depassivation occurred at higher anodic overpotentials, however, at more numerous sites (i.e. metastable-like pits) resulting in a gradual increase in current density (the summation of the various metastable-like pit contributions). Therefore, depassivation occurs at fewer but more vulnerable pit initiation sites for wrought 316L, whereas WAAM 316LSi contains a higher density of less vulnerable initiation sites. The sulfide inclusions present in the wrought 316L are well-known to act as pit initiation sites in stainless steels[59]. The size of MnS inclusions has been shown to be of importance. Steward and Williams[60] estimated that the minimum size required to have an impact on pitting is between 0.25 μm and 1 μm. The MnS sub-inclusions detected in this study (Supplementary Fig. 2) are below this threshold (<0.18 μm), indicating that they do not play a role in pitting.

Therefore, the absence of significant sulfide inclusions within the WAAM 316LSi microstructure is responsible for the higher E_{trans}. Similar effects have been reported in other studies that focused on powder-based AM of stainless steels, where the
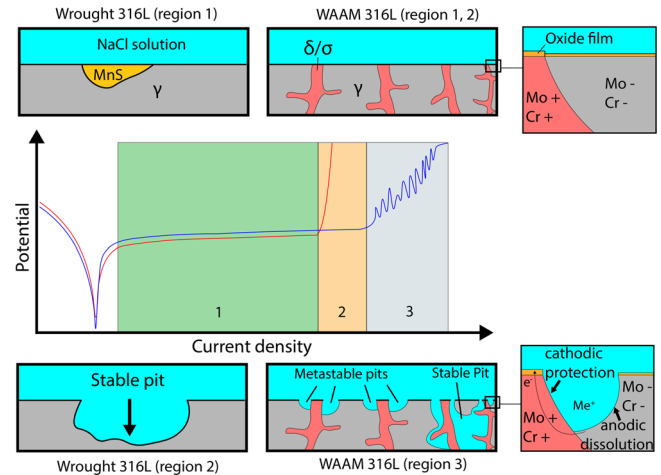
absence of sulfide inclusions within the AM microstructure led to higher E_{trans}[24,25,61,62]. The depassivation potential is lower near the sulfide inclusions causing the current density to rapidly increase at lower potential than for the WAAM material. The high metastable-like activity for WAAM 316LSi was related to the presence of the secondary phases as observations show the corrosion feature shape is closely linked to the secondary phase microstructure network, as seen in Fig. 6. Loss of passivity might preferentially occur at the phase boundaries because of the local oxide film instability owing to the different Cr content in the different phases leading to different oxide film thicknesses. Marcus et al.[63] remarked that oxide layers are preferentially disrupted at defect sites such as grain boundaries and steps when exposed to a corrosive environment.

It was also reported that the passive film itself depends on the crystalline structure of the material upon which it grows and depends on the chemical composition of the substrate metal (Cr content in the case of stainless steels). This explains the higher metastable-like pit density for WAAM 316LSi considering the high concentration of phase boundaries within the WAAM 316LSi microstructure. Interestingly, preferential attack at the ferrite/austenite interphase boundaries in wire-based and powder-based AM stainless steels was previously reported in several studies[30,33,64]. At higher anodic overpotentials, the frequency of metastable pit events increases as well as their dissolution rate which results in the slow and noisy current density increase observed in Fig. 5 and as illustrated in Fig. 8. Preferential dissolution of the austenite immediately adjacent to sigma was observed while the secondary phase remained protected. This can be attributed to a micro-galvanic coupling caused by the dealloying of Cr and Mo elements between the matrix and secondary phases, i.e. ferrite and/or sigma phases. EDX line scans provide an estimation of the ferrite phase with 24 wt% Cr and 3.9 wt% Mo, as well as the sigma phase with 25 wt% Cr and 5.6 wt% Mo, both of which are higher than that in the austenite (17.8 wt% Cr and Mo <2.4 wt%). This generates a local potential difference and galvanic coupling, leading to the accelerated dissolution of the austenite immediately adjacent to these secondary phases and the cathodic protection of the ferrite or sigma phase, as illustrated in Fig. 8. Moreover, the galvanic driving force is stronger for increasing composition differences, which explains why the current density increase is steeper for HT due to stronger Mo segregation, as seen in Fig. 5.

Based on the findings of this study, the temperature range of 600–900 °C should be avoided while heat treating WAAM 316L SS, as it leads to the precipitation of sigma and reduces corrosion resistance. Low-temperature stress relief heat treatment, below
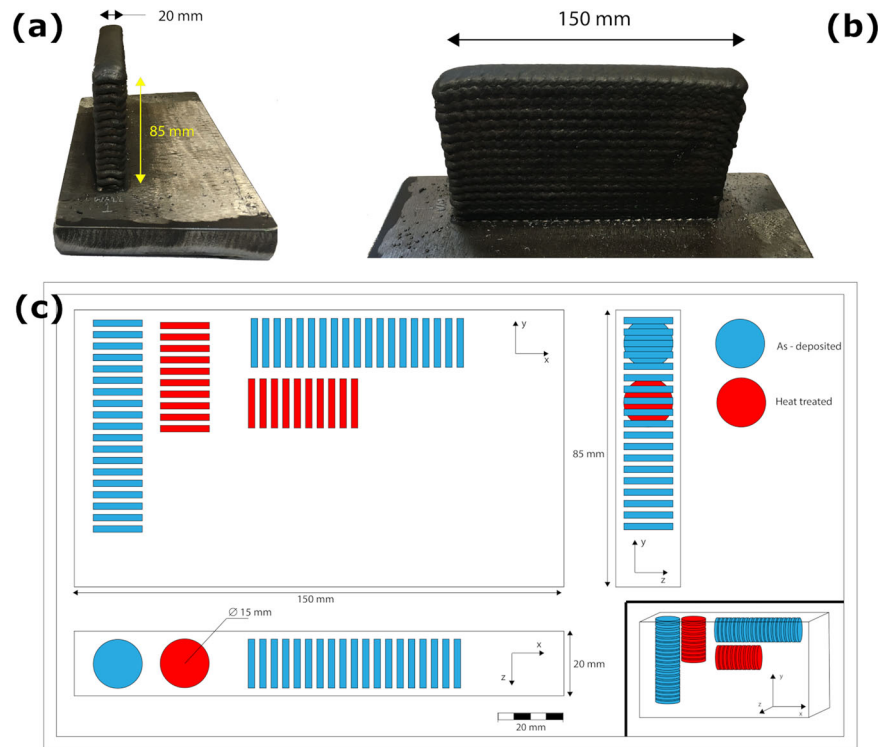
Fig. 9 WAAM wall and specimen extraction layout. a, b The deposited 316LSi WAAM wall before specimen extraction, (y, z), (x, y) orientations, respectively. **c** Specimen extraction layout.

450 and 600 °C, is a viable alternative to avoid sigma and further elemental segregation. Another option is a novel solution annealing HT well above the sigma forming range, typically above 1050 °C[65], although this must be carefully considered, as it may induce grain growth, which could have a detrimental effect on mechanical properties.

- Conventional stress relief HT (a 2 h dwell at 900 °C) is not suitable for WAAM 316LSi due to its tendency to precipitate sigma phase. Attributed to the thermal cycles during WAAM deposition initiating a partial ferrite-sigma transformation and a subsequent complete transformation of ferrite into sigma phase during the HT, which leads to an inferior corrosion performance when compared to the as-deposited WAAM 316LSi.
- Sub-micron silicate inclusions were uniformly dispersed in the WAAM 316LSi microstructure. These silicates were enriched in Mn and S, which rapidly form during solidification preventing the formation of larger sulfide inclusions. The absence of sulfides within the AD WAAM 316LSi influenced pit initiation during anodic polarisation in comparison to the conventional wrought 316L, resulting in a higher E_{trans} for WAAM 316LSi.
- WAAM 316LSi has a less stable oxide film than wrought 316L as characterised by an extensive metastable-like activity at high anodic overpotentials. This instability was attributed to the presence of secondary phases, i.e. ferrite and sigma phases, causing elemental segregation of Cr and Mo and micro-galvanic coupling resulting in the selective dissolution of the austenite phase.

METHODS

Wall deposition and specimen extraction

A WAAM wall of 150 mm × 85 mm × 20 mm was deposited using a Fronius TPS 4000 CMT advanced power source and a Fanuc ArcMate 120ic robot (see Fig. 9). The torch scanning strategy was

an oscillated pattern along the width and deposition parameters are listed in Supplementary Table 1.

The deposition interpass temperature was monitored and maintained under 400 °C to avoid the precipitation of undesirable phases. The feedstock used was a 1.0 mm diameter LNM ER316LSi (316LSi) welding wire from Lincoln Electric, which is conventionally used for welding of 316L substrates, its composition can be seen in Supplementary Table 2, together with the composition of the as-deposited build. This welding wire is riche in Si that improves deoxidisation of the melt and better provides weldability by decreasing the viscosity of the molten metal. Test specimens were extracted from the wall according to Fig. 9c. Specimens denoted H (for Horizontal) had a surface of interest parallel to the (z, x) plane and specimens denoted V (for Vertical) had their surface of interest parallel to the (y, z) plane. A stress relief heat treatment was applied to some specimens (in red). The heat treatment consisted of a 2 h dwell at 900 °C followed by air-cooling to room temperature. Heat-treated specimens are referred to as HT H and HT V depending on the orientation of their surface of interest. Likewise, as-deposited horizontal and vertical specimens were identified as, AD H and AD V, respectively.

Material characterisation

Specimen surface preparation involved grinding using SiC papers of 120, 360, 600, 1200 and 2500 grit and polishing using an oil-based 1 μm diamond suspension. Specimens were chemically etched using Kalling's reagent for a few seconds. The microstructure was studied using an Olympus optical microscope and a ZEISS Sigma Scanning Electron Microscope (SEM) using secondary electron (SE) and backscattered electron modes. Semi-quantitative Energy Dispersive X-ray (EDX) analysis was performed using the SEM. The EDX electron beam was calibrated using a cobalt standard specimen. Correction factors for Cr, Mo and Ni elements were calculated based on the analysis of known references containing these elements in comparable proportion. The

correction factor for Cr was determined using a UNS S31600 reference. Correction factors for Mo and Ni were determined using an Alloy C276 (UNS N10276) reference. Electron Backscatter Diffraction (EBSD) was also performed. Specimens were finely polished using a colloidal silica suspension (0.04 μm) and carefully cleaned with acetone and a microfibre cloth prior to the analysis. The ferrite phase content was determined using a Fischer FMP30 Feritscope.

Sigma phase estimation

The assessment of the sigma phase content is facilitated by its distinctive non-ferromagnetic property, which distinguishes it from ferrite. The Feritscope, a magnetic-based instrument, solely quantifies the ferrite content. The NaOH electro-etching method reveals secondary phases comprising both ferrite and sigma. Consequently, the sigma content may be approximated by computing the disparity between the secondary phase and the ferrite content measured by Feritscope. The SEM is employed to determine the secondary phase content by utilising a thresholding technique. The secondary phase content was evaluated for both AD and HT conditions, with the data obtained for the AD specimens exhibiting a high degree of concurrence with the Feritscope data, as indicated in Supplementary Table 2. The minor 0.7% divergence between the two sets of data could be due to the presence of the sigma phase or the threshold overestimating the secondary phase. Nonetheless, these results remain sufficiently precise and may be used to validate measurements obtained from HT specimens. However, the final estimation of the sigma content is only an approximation, since it is not obtained via direct measurement, and, therefore, is prone to the accumulation of potential errors. The secondary phase was determined from 13 SEM images on vertical specimens and across the entirety of a layer for both conditions. Each SEM image covered a surface area of 1100 μm × 380 μm for a total of 5.4 mm^2. Three Feritscope measurements were taken close to the SEM analysed region for comparison.

Electrochemical testing

Specimens were polished to a 3 μm finish and cleaned in an ultrasonic bath filled with acetone for 10 min. After cleaning, specimens were left in the ambient laboratory air for at least 24 h to condition the surface before corrosion testing. Test specimens were then enclosed in a test cell equipped with a PTFE gasket to prevent crevice corrosion with a working electrode surface of 1.33 cm^2. The 3.5 wt% NaCl test solution (volume: 300 mL) was prepared with deionised water and laboratory-grade reagents. Linear polarisation resistance (LPR), electrochemical impedance spectroscopy (EIS) and potentiodynamic polarisation (PDP) were performed after recording the open circuit potential (OCP) for 1 h when stabilisation had occurred. Triplicate PDP measurements were performed to ensure reproducibility. In the interest of clarity, Fig. 5 displays only one representative polarisation per experimental condition, while the complete set of measurements can be found in Supplementary Fig. 4. The counter electrode was a graphite rod, and the reference electrode was a silver/silver chloride (Ag/AgCl, 3.5 M KCl solution) electrode. The test solution was maintained at ambient laboratory conditions. The LPR potential offset relative to OCP was ± 20 mV with a scan rate of 0.125 mV s^{-1}. For EIS, the applied sinusoidal potential was 10 mV$_{rms}$ and frequencies ranged between 10^5 Hz and 10^{-2} Hz. Standard procedures for the selection of equivalent circuit best-fit using the Gamry Echem Analyst software were followed: (i) the chi-squared (x^2) error was suitably minimised ($x^2 \leq 10^{-3}$) and (ii) the errors associated with each element were ranged between 0 and 5%. For PDP, the potential was swept from −300 mV vs. OCP in the electropositive direction until the current density reached 1000 μA cm^{-2} at a scan rate of 0.5 mV s^{-1}. Post electrochemical

testing, specimens were cleaned in an ultrasonic bath filled with acetone for 30 min and surfaces assessed using optical microscopy (OM) and/or SEM. Surfaces were characterised before and after the electrochemical tests to ensure no crevice corrosion occurred. The occurrence of depassivation events, characterised by oxide film breakdowns, during PDP was investigated. Quantification was achieved through the detection of visible surface features using an image segmentation tool implemented in Matlab. Each feature was deemed as the outcome of a depassivation event and was assimilated to a metastable-like pit, whereby even stable pits were deemed metastable-like to ensure simplicity and focus on depassivation events. The density of metastable-like pits was calculated by dividing the number of visible features on the surface by the total exposed surface area.

DATA AVAILABILITY

The datasets generated during and/or analysed during the current study are available from the corresponding author on reasonable request.

REFERENCES

1. Frazier, W. E. Metal additive manufacturing: a review. *J. Mater. Eng. Perform.* **23**, 1917–1928 (2014).
2. Cunningham, C. R., Flynn, J. M., Shokrani, A., Dhokia, V. & Newman, S. T. Invited review article: strategies and processes for high quality wire arc additive manufacturing. *Addit. Manuf.* **22**, 672–686 (2018).
3. Wu, B. T. et al. A review of the wire arc additive manufacturing of metals: properties, defects and quality improvement. *J. Manuf. Process.* **35**, 127–139 (2018).
4. Jin, W. et al. Wire arc additive manufacturing of stainless steels: a review. *Appl. Sci.* **10**, 1563 (2020).
5. Taşdemir, A. & Nohut, S. An overview of wire arc additive manufacturing (WAAM) in shipbuilding industry. *Ships Offshore Struct.* **16**, 797–814 (2020).
6. Katou, M., Oh, J., Miyamoto, Y., Matsuura, K. & Kudoh, M. Freeform fabrication of titanium metal and intermetallic alloys by three-dimensional micro welding. *Mater. Des.* **28**, 2093–2098 (2007).
7. Skiba, T., Baufeld, B. & Biest, Ovd Microstructure and mechanical properties of stainless steel component manufactured by shaped metal deposition. *ISIJ Int.* **49**, 1588–1591 (2009).
8. Baufeld, B., Biest, Ovd & Gault, R. Microstructure of Ti-6Al-4V specimens produced by shaped metal deposition. *Int. J. Mater. Res.* **100**, 1536–1542 (2009).
9. Baufeld, B. & van der Biest, O. Mechanical properties of Ti-6Al-4V specimens produced by shaped metal deposition. *Sci. Technol. Adv. Mater.* **10**, 015008 (2009).
10. Wang, F., Williams, S., Colegrove, P. & Antonysamy, A. A. Microstructure and mechanical properties of wire and arc additive manufactured Ti-6Al-4V. *Metall. Mater. Trans. A* **44**, 968–977 (2013).
11. Wang, J. F., Sun, Q. J., Wang, H., Liu, J. P. & Feng, J. C. Effect of location on microstructure and mechanical properties of additive layer manufactured Inconel 625 using gas tungsten arc welding. *Mater. Sci. Eng. A* **676**, 395–405 (2016).
12. Almeida, P. & Williams, S. *Innovative process model of Ti-6Al-4V additive layer manufacturing using cold metal transfer (CMT)* (Conference Proceeding at the Twenty-First Annual International Solid Freeform Fabrication Symposium, Austin, US, 2010). https://doi.org/10.26153/tsw/15162.
13. Chen, X. et al. Microstructure and mechanical properties of the austenitic stainless steel 316L fabricated by gas metal arc additive manufacturing. *Mater. Sci. Eng. A* **703**, 567–577 (2017).
14. Rodriguez, N. et al. Wire and arc additive manufacturing: a comparison between CMT and TopTIG processes applied to stainless steel. *Weld. World.* **62**, 1083–1096 (2018).
15. Wang, L. L., Xue, J. X. & Wang, Q. Correlation between arc mode, microstructure, and mechanical properties during wire arc additive manufacturing of 316L stainless steel. *Mater. Sci. Eng. A-Struct. Mater. Prop. Microstruct. Process.* **751**, 183–190 (2019).
16. Wu, W. et al. Forming process, microstructure, and mechanical properties of thin-walled 316L stainless steel using speed-cold-welding additive manufacturing. *Metals* **9**, 109 (2019).
17. Wu, W., Xue, J., Zhang, Z. & Yao, P. Comparative study of 316L depositions by two welding current processes. *Mater. Manuf. Processes* **34**, 1502–1508 (2019).

18. Lee, S. H. CMT-based wire arc additive manufacturing using 316L stainless steel: effect of heat accumulation on the multi-layer deposits. *Metals* **10**, 278 (2020).

19. Yang, K., Wang, Q., Qu, Y., Jiang, Y. & Bao, Y. Microstructure and corrosion resistance of arc additive manufactured 316L stainless steel. *J. Wuhan Univ. Technol.-Mat. Sci. Ed.* **35**, 930–936 (2020).

20. Cunningham, C. R., Dhokia, V., Shokrani, A. & Newman, S. T. Effects of in-process LN$_2$ cooling on the microstructure and mechanical properties of type 316L stainless steel produced by wire arc directed energy deposition. *Mater. Lett.* **282**, 128707 (2021).

21. Palmeira Belotti, L. et al. Microstructural characterisation of thick-walled wire arc additively manufactured stainless steel. *J. Mater. Process. Technol.* **299**, 117373 (2022).

22. Wang, C., Zhu, P., Lu, Y. H. & Shoji, T. Effect of heat treatment temperature on microstructure and tensile properties of austenitic stainless 316L using wire and arc additive manufacturing. *Mater. Sci. Eng. A* **832**, 142446 (2022).

23. Zhong, Y., Zheng, Z., Li, J. & Wang, C. Fabrication of 316L nuclear nozzles on the main pipeline with large curvature by CMT wire arc additive manufacturing and self-developed slicing algorithm. *Mater. Sci. Eng. A* **820**, 141539 (2021).

24. Sander, G. et al. On the corrosion and metastable pitting characteristics of 316L stainless steel produced by selective laser melting. *J. Electrochem. Soc.* **164**, C250–C257 (2017).

25. Man, C. et al. The enhancement of microstructure on the passive and pitting behaviors of selective laser melting 316L SS in simulated body fluid. *Appl. Surf. Sci.* **467-468**, 193–205 (2019).

26. Laleh, M. et al. On the unusual intergranular corrosion resistance of 316L stainless steel additively manufactured by selective laser melting. *Corros. Sci.* **161**, 108189 (2019).

27. Zhou, C. et al. Enhanced corrosion resistance of additively manufactured 316L stainless steel after heat treatment. *J. Electrochem. Soc.* **167**, 141504 (2020).

28. Queguineur, A., Rückert, G., Cortial, F. & Hascoët, J. Y. Evaluation of wire arc additive manufacturing for large-sized components in naval applications. *Weld. World.* **62**, 259–266 (2018).

29. Wen, D., Long, P., Li, J., Huang, L. & Zheng, Z. Effects of linear heat input on microstructure and corrosion behavior of an austenitic stainless steel processed by wire arc additive manufacturing. *Vacuum* **173**, 109131 (2019).

30. Chen, X., Li, J., Cheng, X., Wang, H. & Huang, Z. Effect of heat treatment on microstructure, mechanical and corrosion properties of austenitic stainless steel 316L using arc additive manufacturing. *Mater. Sci. Eng. A* **715**, 307–314 (2018).

31. Villanueva, D. M. E., Junior, F. C. P., Plaut, R. L. & Padilha, A. F. Comparative study on sigma phase precipitation of three types of stainless steels: austenitic, superferritic and duplex. *Mater. Sci. Technol.* **22**, 1098–1104 (2006).

32. Padilha, A. F. & Rios, P. R. Decomposition of austenite in austenitic stainless steels. *ISIJ Int.* **42**, 325–327 (2002).

33. Ziętala, M. et al. The microstructure, mechanical properties and corrosion resistance of 316L stainless steel fabricated using laser engineered net shaping. *Mater. Sci. Eng. A* **677**, 1–10 (2016).

34. Guilherme, L. H., Benedetti, A. V., Fugivara, C. S., Magnabosco, R. & Oliveira, M. F. Effect of MAG welding transfer mode on sigma phase precipitation and corrosion performance of 316L stainless steel multi-pass welds. *J. Mater. Res. Technol.* **9**, 10537–10549 (2020).

35. Li, C., Liu, Z. Y., Fang, X. Y. & Guo, Y. B. Residual stress in metal additive manufacturing. *Proced. CIRP* **71**, 348–353 (2018).

36. Mukherjee, T., Zhang, W. & Debroy, T. An improved prediction of residual stresses and distortion in additive manufacturing. *Comput. Mater. Sci.* **126**, 360–372 (2017).

37. Wu, A. S., Brown, D. W., Kumar, M., Gallegos, G. F. & King, W. E. An experimental investigation into additive manufacturing-induced residual stresses in 316L stainless steel. *Metall. Mater. Trans. A* **45**, 6260–6270 (2014).

38. *ASM Handbook. Volume 4, Heat Treating* (ASM International, Materials Park, OH, 1991).

39. Singh, R. *Welding Corrosion-Resistant Alloys: Stainless Steel. 2nd edn*, book section 6, 239–262 (Butterworth-Heinemann, 2016).

40. Folkhard, E. *Welding Metallurgy of Stainless Steels* (Springer Science & Business Media, 2012).

41. Hsieh, C.-C. & Wu, W. Overview of intermetallic sigma (σ) phase precipitation in stainless steels. *ISRN Metall.* **2012**, 1–16 (2012).

42. Raghunathan, V. S., Seetharaman, V., Venkadesan, S. & Rodriguez, P. The influence of post weld heat treatments on the structure, composition and the amount of ferrite in type 316 stainless steel welds. *Metall. Trans. A* **10**, 1683–1689 (1979).

43. Kang, Y.-B., Kim, H. S., Zhang, J. & Lee, H.-G. Practical application of thermodynamics to inclusions engineering in steel. *J. Phys. Chem. Solids* **66**, 219–225 (2005).

44. Liu, C.-s et al. Influence of FeO and sulfur on solid state reaction between MnO-SiO2-FeO oxides and an Fe-Mn-Si solid alloy during heat treatment at 1473 K. *Int. J. Miner. Metall. Mater.* **22**, 811–819 (2015).

45. Wang, C., Zhu, P., Wang, F., Lu, Y. H. & Shoji, T. Anisotropy of microstructure and corrosion resistance of 316L stainless steel fabricated by wire and arc additive manufacturing. *Corros. Sci.* **206**, 110549 (2022).

46. Suzuki, M., Yamaguchi, R., Murakami, K. & Nakada, M. Inclusion particle growth during solidification of stainless steel. *ISIJ Int.* **41**, 247–256 (2001).

47. Diederichs, R. & Bleck, W. Modelling of manganese sulphide formation during solidification, part I: Description of MnS formation parameters. *Steel Res. Int.* **77**, 202–209 (2006).

48. Le, V. T., Mai, D. S. & Paris, H. Influences of the compressed dry air-based active cooling on external and internal qualities of wire-arc additive manufactured thin-walled SS308L components. *J. Manuf. Process.* **62**, 18–27 (2021).

49. Le, V. T., Mai, D. S., Doan, T. K. & Paris, H. Wire and arc additive manufacturing of 308L stainless steel components: Optimization of processing parameters and material properties. *Eng. Sci. Technol. Int. J.* **24**, 1015–1026 (2021).

50. Gabrielli, C. Use and Application of Electrochemical Impedance Techniques. Technical Report, Schlumberger Technologies-Instruments Division (1990).

51. Trethewey, K. R. & Chamberlain, J. *Corrosion: For Science and Engineering.* 2nd edn (Longman, London, 1995).

52. Boissy, C., Ter-Ovanessian, B., Mary, N. & Normand, B. Correlation between predictive and descriptive models to characterize the passive film - study of pure chromium by electrochemical impedance spectroscopy. *Electrochim. Acta* **174**, 430–437 (2015).

53. Brug, G. J., van den Eeden, A. L. G., Sluyters-Rehbach, M. & Sluyters, J. H. The analysis of electrode impedances complicated by the presence of a constant phase element. *J. Electroanal. Chem. Interfacial Electrochem.* **176**, 275–295 (1984).

54. Hsu, C. H. & Mansfeld, F. Technical note: Concerning the conversion of the constant phase element parameter Y0 into a capacitance. *Corrosion* **57**, 747–748 (2001).

55. Hirschorn, B. et al. Determination of effective capacitance and film thickness from constant-phase-element parameters. *Electrochim. Acta* **55**, 6218–6227 (2010).

56. Yi, Y., Cho, P., Al Zaabi, A., Addad, Y. & Jang, C. Potentiodynamic polarization behaviour of AISI type 316 stainless steel in NaCl solution. *Corros. Sci.* **74**, 92–97 (2013).

57. Frankel, G. S., Stockert, L., Hunkeler, F. & Boehni, H. Metastable pitting of stainless steel. *Corrosion* **43**, 429–436 (1987).

58. Laycock, N. J. & Newman, R. C. Localised dissolution kinetics, salt films and pitting potentials. *Corros. Sci.* **39**, 1771–1790 (1997).

59. Ryan, M. P., Williams, D. E., Chater, R. J., Hutton, B. M. & McPhail, D. S. Why stainless steel corrodes. *Nature* **415**, 770–774 (2002).

60. Stewart, J. & Williams, D. E. The initiation of pitting corrosion on austenitic stainless steel: on the role and importance of sulphide inclusions. *Corros. Sci.* **33**, 457–474 (1992).

61. Chao, Q. et al. On the enhanced corrosion resistance of a selective laser-melted austenitic stainless steel. *Scr. Mater.* **141**, 94–98 (2017).

62. Lass, E. A. et al. Formation of the Ni3Nb δ-phase in stress-relieved Inconel 625 produced via laser powder-bed fusion additive manufacturing. *Metall. Mater. Trans. A* **48**, 5547–5558 (2017).

63. Marcus, P. & Maurice, V. Atomic-level characterization in corrosion studies. *Philos. Trans. A Math. Phys. Eng. Sci.* **375**, 20160414 (2017).

64. Tarasov, S. Y. et al. Microstructural evolution and chemical corrosion of electron beam wire-feed additively manufactured AISI 304 stainless steel. *J. Alloy. Compd.* **803**, 364–370 (2019).

65. Kong, D. et al. Mechanical properties and corrosion behavior of selective laser melted 316L stainless steel after different heat treatment processes. *J. Mater. Sci. Technol.* **35**, 1499–1507 (2019).

AUTHOR CONTRIBUTIONS

C.P.: conceptualisation and methodology, original manuscript writing, experimental work, data interpretation. J.W.: conceptualisation and methodology, data interpretation, manuscript review and editing. A.A.: manufacturing insight - WAAM wall deposition, specimens extraction and heat treatment. Y.W. and Q.L.: corrosion data interpretation, manuscript review and editing.

COMPETING INTERESTS

The authors declare no competing interests.

ADDITIONAL INFORMATION

Supplementary information The online version contains supplementary material available at https://doi.org/10.1038/s41529-023-00359-0.

Correspondence and requests for materials should be addressed to Corentin Penot.

Reprints and permission information is available at http://www.nature.com/reprints

Publisher's note Springer Nature remains neutral with regard to jurisdictional claims in published maps and institutional affiliations.